Comparative Study of the Mineralogy and Chemistry Properties of Elephant Bones: Implications during Diagenesis Processes

Luis Monasterio-Guillot [1,2], **Laura Crespo-López** [1], **Alejandro B. Rodríguez Navarro** [1] **and Pedro Álvarez-Lloret** [1,3,*]

1   Department of Mineralogy and Petrology, University of Granada, 18071 Granada, Spain
2   Institut des Sciences de la Terre, University of Grenoble Alpes, ISTerre, 38000 Grenoble, France
3   Department of Geology, University of Oviedo, 33005 Oviedo, Spain
*   Correspondence: pedroalvarez@uniovi.es

Abstract: Elephants are currently the largest terrestrial mammals, along with their extinct ancestor the mammoth. These species are of great interest due to their geographic distribution and ecological importance. However, the bone mineral characteristics of their skeleton as well as their alteration during burial processes over millions of years have been poorly investigated. In the current research, we analyzed the compositional and structural mineral properties of different types (i.e., long and flat bones) of elephant and mammoth bones. For this purpose, we performed a comparative study between these bone types using complementary analytical techniques based on X-ray diffraction, thermogravimetry, Fourier transform infrared spectroscopy, scanning electron microscopy, and inductively coupled plasma spectroscopic analysis. The chemical composition of the samples shows a relative loss of a considerable percentage of water and organic matter components for the fossilized bone, accompanied by a higher bone mineralization degree and the presence of other crystalline phases (i.e., calcite and pyrite) related to a certain degree of diagenesis alteration. Our results also show a variation in the crystalline properties of mammoth bone related to the recrystallization process during the dissolution–precipitation transformation through diagenetic burial. This research provides relevant information for understanding the mineral properties of different types of bones and their possible changes during diagenesis.

Keywords: bones; mineralization; elephant; mammoth; fossilized; chemical composition; crystallinity

1. Introduction

Elephants are the largest terrestrial living mammals. Several elephant species, such as the African elephant (*Loxodonta africana*), suffered huge population declines in recent decades due to habitat loss and poaching for the illegal ivory trade [1,2]. The International Union for Conservation of Nature (IUCN) listed this species in the Red List of Threatened Species as globally Vulnerable (VU) to extinction [3]. The extinct woolly mammoth (*Mammuthus primigenius*) is the closest relative of recent elephant species [4,5]. Similar to the case of the current decline in the modern elephant, the extinction of mammoth species could be due to overhunting by the *Homo sapiens* [6,7].

Both Elephantidae species, *Loxodonta africana* and *Mammuthus primigenius*, were investigated during recent decades due to their relevance and distribution from an ecological and demographical (e.g., population behavior, geographical occurrence) as well as a socioeconomic (e.g., illegal trade of body parts, such as ivory) point of views [1,2,8,9]. However, few studies were performed on the skeletal structures of these animals and the comparison of recent and fossil bones of both species. An elephant's body is a hundred thousand times heavier than that of a hamster and, therefore, its skeleton has to withstand its body weight. Galileo Galilei was probably the first scientist to publish in his *Dialogues* the effects of body weight on the animal skeleton, which is exposed to loading and bending as the size of the

animal increases, and, thus, its bone morphology and physical–chemical properties have to change accordingly [10].

Bone is a composite material made of an organic matrix (mainly composed of type I collagen fibrils) and an inorganic phase (i.e., nanometer-sized carbonated apatite that derives from hydroxyapatite) hierarchically organized in the bone tissue [11,12]. Bone is a living tissue that is constantly changing through "bone remodeling" that involves the removal of bone mineral by osteoclastic acidification followed by the formation of the bone matrix through the osteoblasts that subsequently become mineralized [13]. Bone remodeling serves to adjust bone architecture to adapt to mechanical loads, as well as to supply ions needed for cell functions. Depending on the type of each bone (e.g., sesamoid, irregular, long, short, or flat bones) and location in the skeleton, its chemical composition and structural organization may vary [14]. In all cases, carbonate molecules substitute phosphate anions in the crystal lattice change the structural properties of hydroxyapatite and modify the mineral properties (solubility) of these bones [15]. On the other hand, after the death of vertebrates, bone materials are the most resistant parts of their bodies to weathering and biological degradation, being susceptible to the diagenesis process and fossilization [16]. To the best of our knowledge, there is no comparative study analyzing the structure and chemistry of elephant and mammoth bones and their possible alterations due to diagenetic processes.

The current research presents a detailed comparative mineralogical and chemical characterization between recent elephant and mammoth using bones from different skeletal locations. Specifically, we employed long and flat bones with different mineral and structural properties [14,17]. To achieve a complete description, we analyzed bone samples through structural (i.e., two-dimensional X-ray diffraction (2D-XRD), X-ray powder diffraction, and scanning electron microscopy) and chemical analyses (i.e., X-ray energy-dispersive and infrared spectroscopies, thermogravimetry, and ICP-OES). Overall, the major aims on this study are: *(i)* to compare the physical–chemical properties of bone mineral from extinct mammoths and recent elephants, which allows us to better understand changes in bone mineral components due to diagenesis; and *(ii)* to combine the information provided by different complementary analytical techniques to reveal and quantify differences at the compositional and structural level between types of bones (e.g., flat and long bones) and their possible changes occurring during diagenetic processes.

2. Materials and Methods

2.1. Materials

Bones of recent elephants (*Loxodonta africana*) were collected from the Cabárceno Natural Park in Cantabria, Spain. Fibula and phalanx bones (mid-diaphysis sections) were selected from a dead 18 years old adult. The cranium of an elephant (parietal section) of the same species that died in the first year of birth was also selected. All bones were stored at room temperature under indoors conditions. Finally, the tibia (mid-diaphysis section) of a woolly mammoth (*Mammuthus primigenius*, ~40 ka BP) was collected from Padul archeological site (Granada, Spain) [18,19]. The archaeological sample was treated following the bone conservation procedures for further characterization studies (no cleaning products were used or exposed in the bone section). Samples were ground (grain size < 200 μm) with a ball mill (Pulverisette 23, Fritsch, Idar-Oberstein, Germany) using low energy vibratory conditions. The heterogeneity of the samples can be justified to characterize the mineralogical and chemical properties of different types of bones in recent elephants, and to study the diagenetic changes on elephant's bones over time.

2.2. Methods

2.2.1. X-ray Powder Diffraction

The identification and calculation of lattice parameters of the mineral phases presented in bones samples was performed by X-ray powder diffraction (XRPD), using a X'Pert PRO diffractometer (PANalytical) with the following instrumental parameters: Cu-Kα radiation,

Ni filter, 40 mA current, 45 kV voltage, 3–70 °2θ scan range, 0.004 °2θ step size, and 29.84 s per step. HighScore Plus 2.2.4 (PANalytical) software was employed to process the XRD patterns by matching the experimental diffraction patterns with those included in the PDF-2 database [20]. Lattice parameters and quantitative analysis were performed by Rietveld analysis [21] using Fullprof software [22] and the crystal structures of hydroxyapatite (HAp) and calcite (Cal) were provided by the American Mineralogist Crystal Structure Database (HAp: reference 0002298; Cal: reference 0000984).

2.2.2. Two-Dimensional (2D) X-ray Diffraction

Longitudinal and transversal sections of long bones (elephant fibula and mammoth tibia) from the midshaft of the diaphysis and sections of elephant phalanx and cranium (i.e., about 1–0.5 cm) were analyzed in transmission mode with an X-ray single-crystal diffractometer (D8 Venture, Bruker, Germany) equipped with a PHOTON area detector, using Mo radiation and a collimator beam size of 0.2 mm in diameter. A quantitative estimation of the degree of alignment of the *c*-axis of apatite crystals in the long bones was determined from the angular breadth of bands displayed in the intensity profile along the Debye–Scherrer ring associated with the (002) reflection of apatite.

2.2.3. Thermogravimetry

Thermogravimetric analyses, TGA (TGA-DSC3+, Mettler Toledo, Columbus, OH, USA) were performed under flowing N_2 using a linear heating rate of 20 °C min^{-1}, from 30 to 950 °C in order to determine different compositional parameters such as water percentage, organic matter, and mineral content.

2.2.4. Infrared Spectroscopy

Chemical composition at molecular level was determined using a Fourier transform infrared (FTIR) spectrometer (model 6200, JASCO Analytical Instruments, Tsukuba, Ibaraki, Japan) equipped with an ATR diamond crystal window (MIRacle Single Reflection ATR, PIKE Technologies). Infrared spectra were recorded at a 2 cm^{-1} resolution over 124 scans. The relative amounts of phosphates, carbonates, and organic matrix were determined from the peak area of the absorption bands associated with their characteristics molecular groups. Peak profile and curve fitting were performed using FITYK 1.3.1 software for data processing and non-linear curve fitting [23]. Pearson's area function was used to fit the bands of the FTIR spectra and calculate the area of the following compositional parameters: *(i)* the relative amount of mineral phosphates (ν_1, ν_3 PO_4; 900–1200 cm^{-1}) to organic matrix (amide I: 1590–1710 cm^{-1}) as PO_4/amide I [17,24,25], *(ii)* the amount of carbonate (ν_3 CO_3; 1390–1450 cm^{-1}) related to the amount of organic matrix as CO_3_1415/amide I [17,25], *(iii)* the amount of carbonate (ν_3 CO_3; 1390–1450 cm^{-1}) related to phosphate (ν_1, ν_3 PO_4; 900–1200 cm^{-1}) bone mineral content (CO_3_1415/PO_4), and *(iv)* the amount of bone mineral carbonate compared to substituted carbonate (ν_2 CO_3; 850–890 cm^{-1}) as CO_3_1415/CO_3_870 [25].

2.2.5. Inductively Coupled Plasma Optical Emission Spectroscopy

The concentration of Ca, Mg, Fe, Na, P, and Sr elements in bone samples was determined by ICP-OES (Perkin Elmer, Optima 8300). For these analyses, 40 mg of bone powder was dissolved in a 0.5 mL solution of 30% H_2O_2 and 0.5 mL 70% HNO_3. After digestion for 48 h, 13 mL of ultrapure MilliQ water (resistivity 18.2 MΩ cm, Millipore, Milwaukee, WI, USA) was added and the sample was filtered.

2.2.6. Scanning Electron Microscopy

The morphology and composition of mammoth bone were characterized by scanning electron microscopy Phenom XL G2 (Thermo Fisher Scientific, Waltham, MA, USA), coupled to an X-ray energy-dispersive spectrometer for chemical micro-analysis, working at an acceleration voltage of 15 kV.

3. Results

3.1. Bone Mineralogy

To determine the mineralogy of the bone samples and the lattice parameters of the unit cell of apatite crystals, the main mineral component of bone, X-ray powder diffraction analyses were performed. Figure 1 displays the diffraction patterns of all bones studied, as well as the RRUFF reference patterns [26] employed for hydroxyapatite and calcite phases identification. No additional crystalline phases are detected in the X-ray diffraction patterns. It should be noted that diffraction peaks corresponding to (211), (112), (300), and (202) crystallographic reflections, present in reference hydroxyapatite XRD pattern, are merged in a single broad diffraction peak in bone samples. On the other hand, the (002), (210), (131), (222), (213), (004), and (511) reflections of hydroxyapatite can be clearly distinguished. However, the diffraction pattern of the mammoth sample shows lower broadening (particularly, for (112), (300), and (202) diffraction peaks of apatite) and the presence of calcite peaks (represented by red arrows in Figure 1). Quantitative analyses performed by the Rietveld method reveal the presence of 2.8 wt% calcite. The observed merging of diffraction peaks is caused by peak broadening due to the nanocrystalline character of bone mineral [27,28]. This peak broadening is highly anisotropic, being smaller for (002) than for (310), due to the elongated shape of bone apatite nanocrystals.
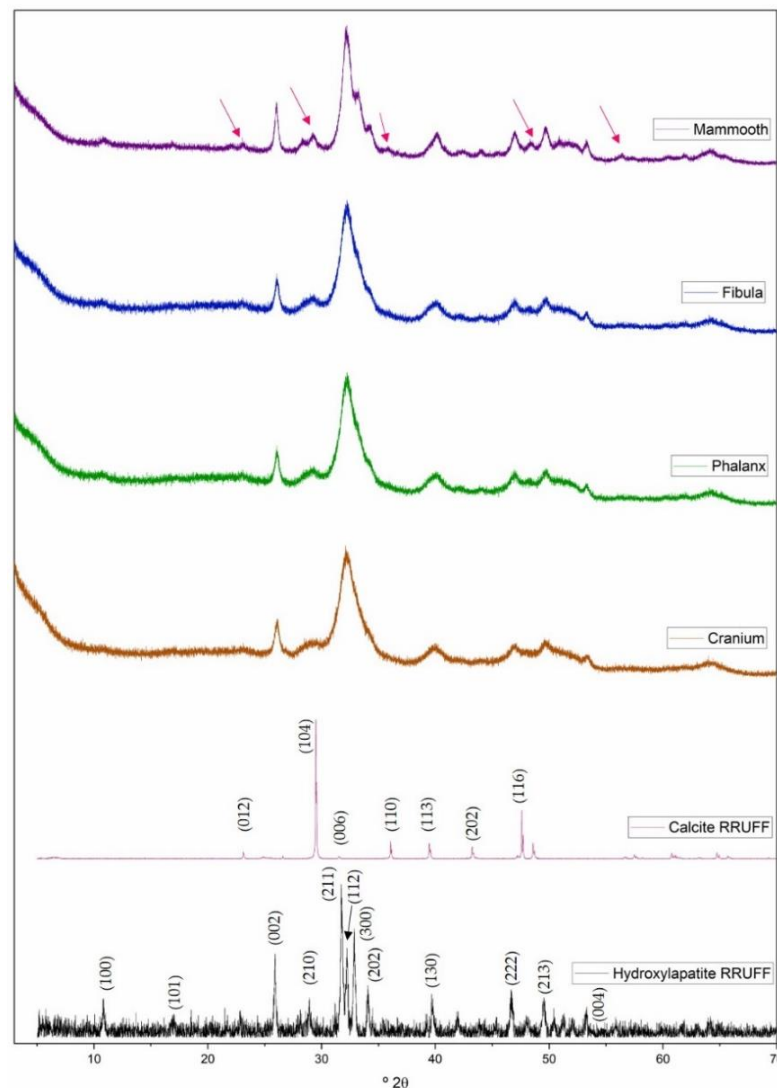
Figure 1. XRD patterns of bone samples and reference patterns of hydroxyapatite and calcite phases. Red arrows in the mammoth diffraction pattern correspond to diffraction peaks of $CaCO_3$.

Lattice parameters for apatite crystals in bone mineral were calculated by the Rietveld method. Furthermore, from the peak broadening, the crystallite size (D) was determined using the Debye–Scherrer equation [9]:

$$D = \frac{K\lambda}{\beta \cos \theta} \tag{1}$$

where D is the crystallite size (nm), K is the Scherrer constant (taken as 0.89), β is the full width at half maximum (FWHM), and θ is the angle of diffraction. The data obtained correspond to an average of the D calculated from all FWHM values integrated in the diffraction pattern.

Table 1 lists the calculated values for D and lattice parameters obtained by XRD analyses for all bone samples. The *a*-lattice parameter of hydroxyapatite shows similar values in all samples, with slight variations considering the third decimal. Cranium shows the highest *a*-lattice parameter, followed by those of the phalanx and the fibula, and the lowest value corresponds to the mammoth sample (difference of 0.0049 Å between the highest and the lowest value). Interestingly, the *c*-lattice parameters show the opposite trend, being the highest for mammoth sample and lowest for the cranium. These findings are evidence that the long bones (i.e., fibula of elephant and tibia of mammoth) exhibit an expansion along the *c*-axis, while the flat bone presents an expansion along the a-axis direction. Regarding the crystallite size of the samples studied, the fibula shows the lower D value ($\Delta \approx -0.28$ nm) than those observed in the rest of the bone samples.

Table 1. Rietveld calculations of lattice parameters (i.e., *a*- and *c*-axes values, expressed in *Angstrom*—**Å**) of hydroxyapatite crystals in bone mineral, the goodness of fitting (GoF) for these crystalline analyses, and the crystallite size (*D*) for all bone samples.

Sample	a (Å)	c (Å)	GoF	Crystallite Size (nm)
Cranium	9.4493	6.8834	4	17.64
Phalanx	9.4474	6.8878	4.1	17.64
Fibula	9.4465	6.8885	4.2	17.35
Mammoth	9.4444	6.8907	4.8	17.63

Two-dimensional X-ray diffraction (2D-XRD) analyses were performed to determine the crystallinity and organization (preferential orientation of hydroxyapatite crystals) of bone mineral. Figure 2 shows the 2D-XRD patterns for a longitudinal section of fibula and cranium bone samples. For the fibula bone, the 2D-XRD patterns show that the intensity of the (002) ring is concentrated in more intense arcs, indicating that a fraction of HAp crystals is preferentially oriented with the *c*-axis parallel to the elongation axis of this bone. On the other hand, the homogenous intensity distribution along the Debye rings in the cranium sample indicates a random orientation of apatite.

Table 2 summarizes the values obtained for the *c*-axis angular spread measure from the distribution of intensity along the Debye ring (gamma scan) and the oriented fraction of HAp crystals considering the total intensity of the diffraction ring for the (002) reflection in the 2D-XRD pattern. For the longitudinal section of fibula and mammoth bone samples, there is a smaller angular spread or scattering (65.43° and 73.37°, respectively) indicating a higher degree of HAp crystals orientation. Considering the relative intensity of the diffraction arc in the (002) direction with respect to the total intensity of the Debye ring, the oriented fraction (OF in Figure 2) can be calculated in the bone samples studied. Thus, the oriented fractions of the HAp crystals in the longitudinal section of fibula and mammoth bone samples are significantly higher ($\Delta > 30$–35%) than the rest of the samples considered in the current study.
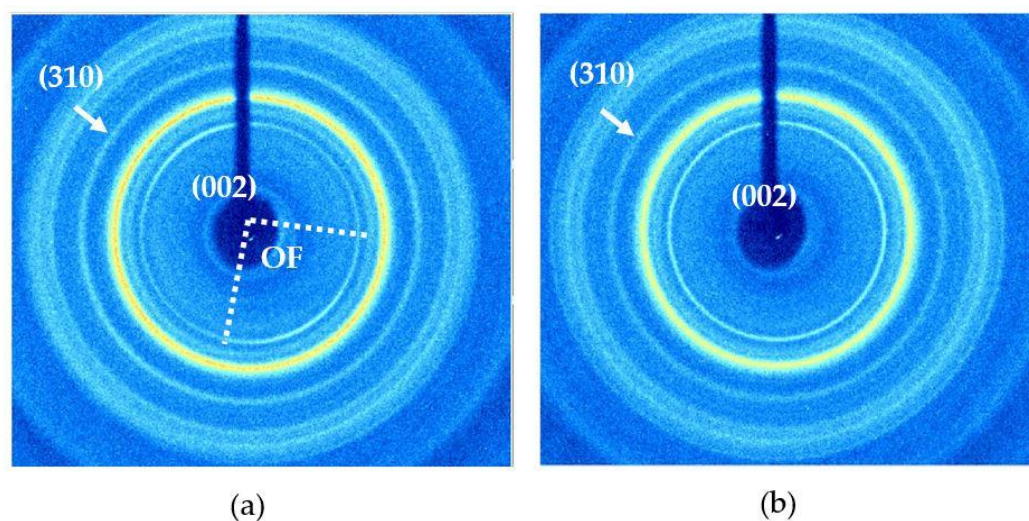
Figure 2. Two-dimensional X-ray diffraction (2D-XRD) patterns from fibula (longitudinal section) (**a**) and cranium (**b**) samples, displaying the peaks and Debye–Scherrer rings for (002) and (310) reflections of hydroxyapatite crystals in bone mineral. OF stands for oriented fraction for angular scattering in the *c*-axis orientation of HAp crystals.

Table 2. Crystals orientation parameters determined by X-ray diffraction in different bone samples obtained by 2D-XRD patterns analyses.

	Cranium	Phalanx	Fibula Trans	Fibula Long	Mammoth
c-axis angular spread (deg)	123.88 ± 5.80	136.03 ± 4.25	114.79 ± 7.11	65.43 ± 3.84	73.38 ± 4.81
Oriented fraction (Rho)	0.244 ± 0.08	0.349 ± 0.08	0.275 ± 0.08	0.622 ± 0.04	0.634 ± 0.10

3.2. Bone Chemistry

Thermogravimetric analyses (TGA) were performed to determine the content of water, organic matter, carbonates, and phosphates in bone samples (Figure 3). First, derivate curves from TGA analyses were plotted in order to clearly define the starting and the ending points of the weight loss in three main identified steps. The first occurs between 25 and 200 °C due to water loss during the dehydration process [27,29,30], a second step up to 580 °C is due to the decomposition of organic components (mainly degradation of collagen) in bone samples [27,30], and finally, a third step up to 850 °C corresponds to carbonate loss included in apatite [22]. Table 3 summarizes the main bone components determined by TGA analyses showing the weight percent of water, organic matter (O.M.), mineral carbonates, and phosphates. Recent elephant bone samples (i.e., cranium, phalanx, and fibula) have the highest content of water (cranium: 10.77 wt%; fibula: 9.1 wt%; phalanx: 8.87 wt%) and organic matter (fibula: 32.53 wt%, phalanx: 32.37 wt%; cranium: 27.5 wt%). On the other hand, the fossil sample of the mammoth presents the lowest content of water and O.M. (water: 6.8 wt%; O.M.: 20.09 wt%) and the highest amount of mineral components (phosphates: 69.66 wt%; carbonates: 3.45 wt%).

Table 3. Thermogravimetric analyses indicating the relative weight loss of water, organic matrix (OM), carbonates, and phosphates in bone samples (see further details in Figure 3).

|	Water (wt%)	O.M. (wt%)	Carbonates (wt%)	Phosphates (wt%)
Cranium	10.77	27.5	2.19	59.54
Phalanx	8.87	32.37	3.09	55.67
Fibula	9.10	32.53	2.53	55.84
Mammoth	6.80	20.09	3.45	69.66
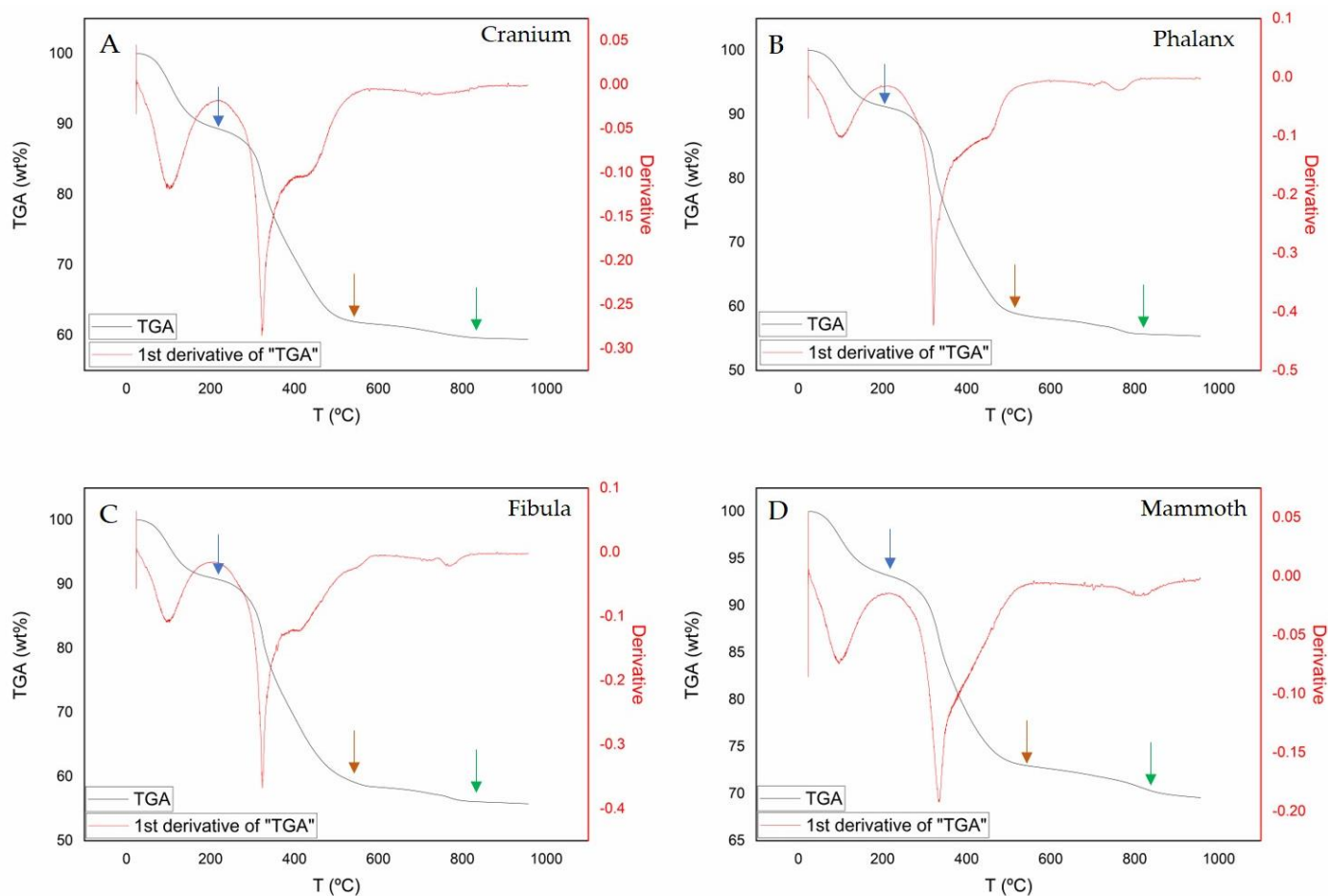
Figure 3. Thermogravimetric traces (black) and first derivate (red) of the bones studied showing three different weigh losses up to 200 °C corresponding to water loss (blue arrows), up to 580 °C corresponding to organic matter (orange arrows), and weigh loss up to 850 °C corresponding to carbonates (green arrows). (**A**) Cranium bone sample. (**B**) Phalanx bone sample. (**C**) Fibula bone sample. (**D**) Mammoth bone sample.

The elemental composition analyses of the bone samples by ICP-OES are presented in Table 4. The results show a higher amount of Ca and Fe content in the mammoth sample compared to the recent elephant bones. In addition, the amount of P and Sr is slightly higher and lower for Na content in the mammoth than in the recent bone samples. Regarding the elephant bone sample analyses, Ca content is higher in the phalanx and fibula, while the cranium shows a slightly lower amount. However, the amount of Mg is considerably higher in the cranium than in both long bones, showing a similar trend for Sr. In addition, the Ca/P ratio shows higher values for the mammoth sample, evidencing a composition above stoichiometric apatite in the bone mineral, related to the presence of diagenetic calcite. Moreover, the ratio of phosphate vs. organic matrix amounts shows a higher mineral content in the mammoth samples (approx. 3.5) with respect to the elephant bones (ranging 1.70–2.16).

Table 4. Elemental composition of bones samples measured by ICP-OES.

Bone	Ca (mmol/L)	Fe (mmol/L)	Mg (mmol/L)	Na (mmol/L)	P (mmol/L)	Sr (mmol/L)	Ca/P
Cranium	574.10	1.31	16.57	21.76	370.64	0.37	1.55
Phalanx	596.23	0.88	10.69	21.70	357.84	0.20	1.67
Fibula	590.32	1.58	10.79	23.80	362.63	0.16	1.63
Mammoth	689.16	5.90	11.82	12.37	379.56	0.59	1.82

Chemical characterization at the molecular level of the bone samples was performed by FTIR analysis. Figure 4a shows representative ATR-FTIR spectra of each bone sample showing absorption bands related to the organic matrix (i.e., amide bands from collagen) and bone mineral components (carbonate and phosphate groups). The FTIR spectrum of mammoth bone displays sharper absorption bands corresponding to the ν_3, ν_4 PO_4 domains.
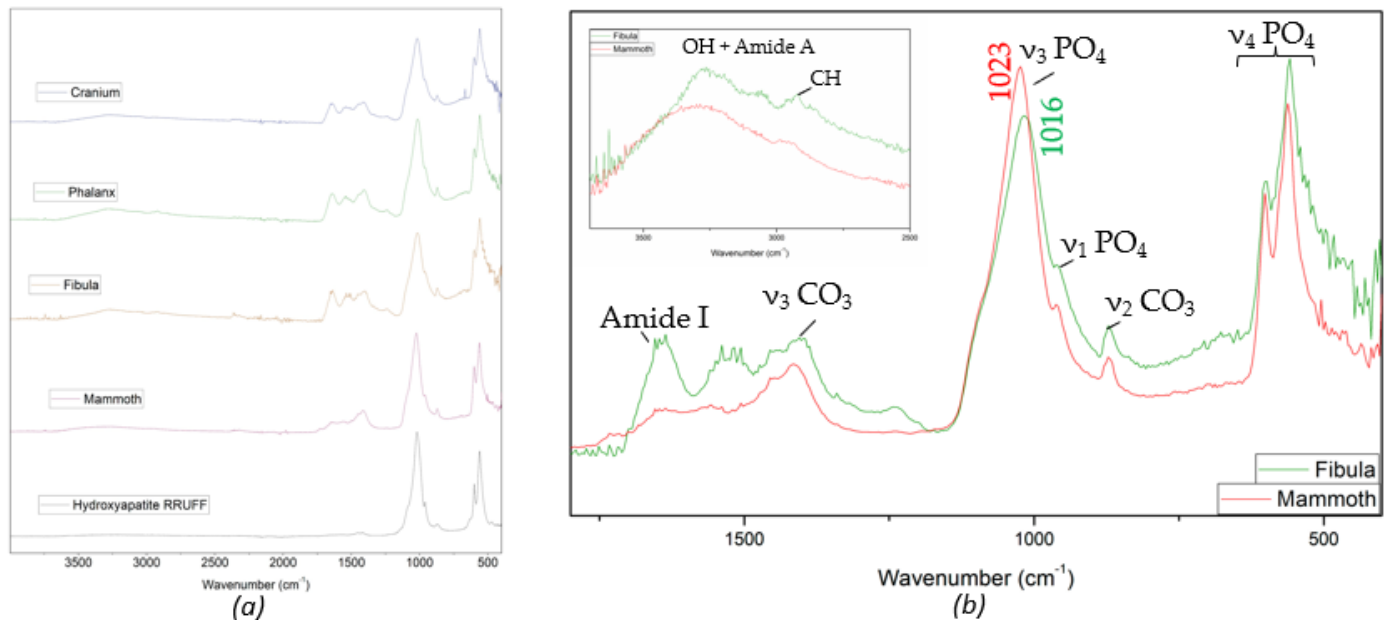
Figure 4. FTIR analyses of bone samples. (**a**) FTIR spectra (450–4000 cm^{-1}) for all studied bone samples and reference spectra of hydroxyapatite obtained from RRUFF database. (**b**) FTIR spectra comparison between recent elephant's fibula (green) and femur of a mammoth (red) displaying characteristic bands corresponding to the main molecular compounds of bone mineral. Inset a detailed section of FTIR spectra (2500–400 cm^{-1}) corresponding to the OH + CH domains.

Furthermore, a marked intensity decrease is observed in amide I band (~1645 cm^{-1}) compared to the recent bone samples. A more detailed comparison between mammoth and fibula bone samples is shown in Figure 4b. The determined FTIR compositional parameters (Table 5) reveal important differences between bone samples. The degree of mineralization (PO_4/amide I ratio) for the mammoth bone is quite high (i.e., 8.938) compared to recent bones. Considering recent bones, the elephant cranium shows the highest ratio, followed by fibula and phalanx ratios. These PO_4/amide I values are correlated to the amount of mineral components (wt% of phosphates) determined by TGA analyses (Table 3). Mammoth bone shows the highest phosphate content (~70 wt%) and the lowest amount of organic matter. For the amount of carbonate related to the organic matrix (CO_3_1415/amide I ratio), the highest ratio is observed for the mammoth bone, just as for the degree of mineralization, followed by the phalanx, and, finally, similar values are observed for the cranium and fibula. In addition, the mammoth bone sample shows a lower CO_3/PO_4 ratio with respect to the modern elephant bones. Finally, the substituted carbonate on bone mineral shows that mammoth samples present the highest carbonate content (i.e., the lowest ratio), followed by the cranium, fibula, and phalanx ratios, where mineral carbonate reaches maximum values with respect to substituted carbonate.

SEM images of mammoth samples (Figure 5) show a cortical bone section, with vascular canals filled by some bone fragments accompanied by pyrite (FeS_2) framboids of size ~15 μm, although this phase could not be detected by XRD. EDS analyses show relative percentages of Ca and P corresponding to apatite mineral composition (EDS analysis 2), and Fe and S elements corresponding to diagenetic pyrite presence (EDS analysis 1).

Table 5. Degree of mineralization (PO_4/amide I), amount of carbonate to organic matrix (CO_3_1415/amide I), carbonate to phosphate mineral content (CO_3_1415/PO_4), and carbonate in the bone mineral and substituted carbonate (CO_3_1415/CO_3_870) determined by ATR-FTIR spectrometric analyses.

	PO_4/Amide I	CO_3_1415/Amide I	CO_3_1415/PO_4	CO_3_1415/CO_3_870
Cranium	4.716	1.686	0.358	5.146
Phalanx	2.686	2.029	0.755	9.388
Fibula	3.219	1.756	0.546	7.908
Mammoth	8.938	2.452	0.274	3.047
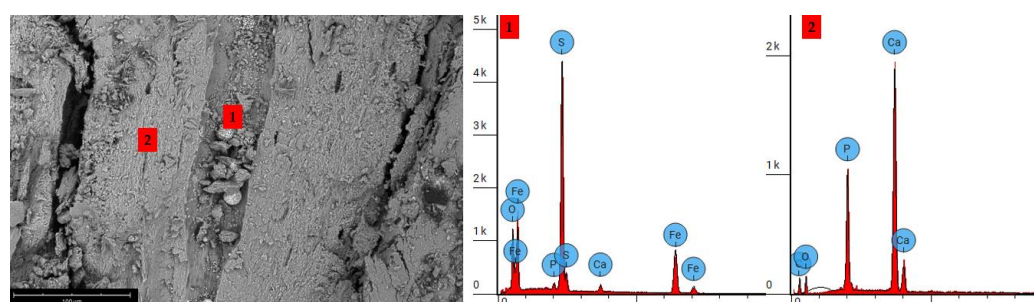
Figure 5. SEM images of mammoth bone samples showing the presence of a vascular canal filled by framboidal pyrites: (1) EDS bone (CaP), (2) pyrite (FeS_2) analyses.

4. Discussion

In the current research, significant differences in bone mineral compositional parameters and crystalline properties are observed for different types of bone (cranium, phalanx, and tibia) from the same species of modern elephant *Loxodonta africana*. The results of the chemical analysis of the flat bone sample show a higher phosphate mineral content relative to the OM, observed by thermogravimetry, and the highest degree of mineralization (i.e., PO4/amide I ratio, obtained by ATR-FTIR analyses, Table 5) with respect to the long bones. The differences observed in mineralization can be caused by the developmental processes during bone tissue formation, varying between intramembranous and endochondral ossification [31]. Comparing recent elephant bone samples, we observe that flat bones (cranium) have higher phosphate and lower carbonate content (and a lower CO_3_1415/PO_4 ratio) than long bones (phalanx and fibula). During bone remodeling, loading is shown to induce mechanosensitivity of cells involved in tissue formation processes in vivo [32,33]. Thus, mechanical stimulation found in different types of bone modulates the activities of osteoblasts and osteoclasts [34]. The biomechanical properties of each bone type within the skeleton may affect the activity of bone matrix components to generate functionally appropriate structures. The differences in mineral characteristics observed in the present study may be related to the specific function (long and flat bones) in the elephant skeleton.

On the other hand, these compositional differences among the various types of bone may also be related to differences in mineral crystalline properties observed by X-ray diffraction techniques (Figures 1 and 2). The microstructural characteristics of apatite in the long bones show a higher degree of orientation (*c*-axis angular scattering) corresponding to the directional bone growth in this type of bone. These findings also support the idea that cortical bones can be divided in woven (immature bone randomly oriented) and lamellar bone (present a *c*-axis organization along the direction planes of the bones) [35] and, therefore, long bones studied here can be classified as mature lamellar bones. There is also a gradual decrease in the angular spread, which indicates that the organization or degree of crystal orientation increases in long bones, while in the flat bone (cranium), this organization is practically random. These differences in their structural characteristics may be due to the different types of mechanical loading to which bones are subjected in the skeleton, as previously observed for several types in other animal models [36].

However, the crystalline characteristics related to the microstructure of the apatite crystals (lattice parameters and crystallite size, Table 1) in the recent elephant bone samples are quietly homogenous. All in all, the structural and compositional properties of different types of bones, such as cranium, fibula, and tibia, adapted to their specific function in the skeleton and to the mechanical forces (especially in large vertebrates, such as the present case of recent and ancestral elephants) that determine their mineral characteristic and structural organization.

The bones recovered from paleontological sites were part of a previous living organism, but their mineral properties underwent significant modifications with their respective in vivo species. Mammoth bone samples were discovered in a late Pleistocene peat bog, located near the town of Padul in the Granada Basin (southern Spain). In the Padul basin, which subsided most during the Quaternary period, two alluvial fan systems of gravel and sand erosional debris were deposited [18]. The sedimentary fill of the basin, which reaches a thickness of at least 107 m, has a lower half consisting of gravels, sands, and lutites of an alluvial fan system, and an upper part, from which the mammoth sample was obtained, formed by peat with layers of sands, silts, and shales of lacustrine or palustrine origin [37,38]. These conditions during the burial process may involve alterations at the physicochemical level to the mineral properties of the bone. Bone mineral is a non-stoichiometric nanocrystalline form of apatite in which substitutions of carbonate molecular groups and numerous traces of other cations, such as F, Na, Mg, Zn and Sr, are commonly present [39]. These bioapatite crystals have a smaller crystal size and compositional variation and, consequently, a higher solubility than geological ones [40], making them more prone to chemical and structural alteration under diagenetic conditions. The results of the current research show a significant compositional variation in the tibia sample of the woolly mammoth (*Mammuthus primigenius*) exposed to diagenetic processes compared with recent elephant bones. The overall analytical data show the loss of a considerable percentage of water and organic matter for the fossilized sample, related to a certain degree of diagenetic alteration. Chemical degradation of collagen during burial can be due to a number of factors, such as time and temperature increase at depth [41], bone mineral density or the presence of fractures [42], microbial attack [43], and the presence of water in the environment [44], among others. This loss of the organic component of bone during diagenetic alteration results in a higher value for phosphate and carbonate compositional parameters (i.e., higher PO_4/amide I and CO_3_1415/amide I values, obtained by ATR-FTIR analyses). Moreover, the increase in mineral phosphate content and the degree of orientation of the apatite along the *c*-axis in the mammoth samples may be due to Ostwald ripening (in which larger crystals absorb the smaller ones), loss of the smaller crystals through dissolution–precipitation (coupled to the presence of secondary phases, such as calcite), or both mechanisms [45–47]. Recent studies show similar effects during ivory diagenesis on mammoths as compared to recent elephant [48,49]. The results also show a lower ratio of carbonate to phosphate mineral in the fossil sample. A similar relationship in the CO_3/PO_4 ratio was also observed in fossilized bones of shark vertebrae [50]. This variation may also be indicative of a diagenetic loss of carbonate during recrystallization and a dissolution of the bone mineral. On the other hand, carbonate groups can be substituted at two different anionic positions in the hydroxyapatite structure at PO_4^{3-} (B-type) and/or OH- (A-type) sites [15,51]. Between these carbonate substitutions, the B-type dominates the apatitic formation of biominerals, whereas the A-type controls the properties of apatitic minerals under non-physiological conditions [52]. It should be considered that possible changes in the type A–B substitution ratio in fossils compared to modern tissues point to the fact that the carbonate component of biogenic phosphates may change during diagenesis [53]. Our results show lower values for the CO_3_1415/CO_3_870 ratio (B-type vs. A + B type and labile carbonate) in fossil bone, which may imply a preferential loss of the structural carbonate substitution of PO_4 probably associated with the apatite dissolution processes of bone mineral during diagenesis. The Ca/P ratios obtained by ICP-OES show much higher levels in the mammoth bones, which may be due to a mineralization alteration

due to these diagenetic processes, as well as the presence of other mineral phases during the dissolution–recrystallization process such as calcite (identified by XRD). In addition, the results obtained show an increased incorporation of cationic elements (such as iron and strontium), the presence of which may be associated with alteration mechanisms in burial environments [45,46]. Moreover, SEM-EDX observations of the mammoth samples also show the remarkable presence of framboidal pyrites in the bone fractures (Figure 5), associated with an early diagenetic process. The precipitation of pyrite during diagenesis occurs in cavities accessible to the fluids (e.g., Haversian canals, osteocyte lacunae), here observed in the bone vascular canals, evidencing a diagenetic process included in an early diagenetic environment and low redox conditions (Fe^{3+} reduces into Fe^{2+}) [54]. The formation of mineral products or phases during burial processes is dependent on locally variable factors including reagent availability, water chemistry, and wettability [55]. In sub-aqueous sedimentary environments, where the oxidation zone is absent, sulfate-reducing bacteria are active, thus, S reacts with Fe to form sedimentary pyrite, with the most common initial textures displaying scattered clusters of framboids. On the other hand, where pH is buffered by chemical species other than CO_2, the availability of CO_2 together with the presence of alkaline earth metals leads to the precipitation of carbonate phases (i.e., mainly calcite and dolomite). This mineral precipitation is common in sedimentary environments such as peat bog with anoxic conditions, which contributes to the preservation of the bones up to the present day [19]. These compositional changes may involve the dissolution and recrystallization of bone tissue or its replacement by other mineral phases characteristic of sedimentary environments [54,56]. Indeed, X-ray diffraction analyses show the presence of a calcium carbonate phase (calcite) in the fossil bone sample. On the other hand, the compositional alteration, in turn, results in a variation of the crystalline properties of the fossil bone (i.e., higher orientation degree and crystallite size of apatite crystals) related to the recrystallization process, together with a possible Ostwald ripening mechanism, during the diagenetic mineral transformation previous mentioned. These microstructural properties were used as one of the parameters to characterize the degree of burial alteration of fossil bones [41,47,57]. These diagenetic alteration processes in bone mineral may depend on various properties related to tissue characteristics (v.gr., anatomical location and type of bone), as well as the burial environment [58]. The current study shows the possible alterations of various types of bone in large mammalian species, but it is shown that within animal groups, there are properties (such as bone density or porosity) that significantly influence the decomposition rates under diagenetic conditions [59]. On the other hand, bone degradation during diagenesis does not follow a simple and predictable pathway, and may present different susceptibility depending on the burial environment. Likewise, there are also numerous environmental factors that determine the state of bone preservation, such as soil pH and Eh, hydrology and/or bone–humic interactions, amongst others [60]. Therefore, the compositional variation and microstructural alterations observed in the mammoth bone are identifiable properties of transformation with respect to bone mineralization in recent elephants (examples of large vertebrates) due to diagenetic alteration processes.

The current study demonstrates how various types of bones, including flat and long bones, of the elephant skeleton have different characteristics at the inorganic and organic chemical level, as well as in the crystallinity and structural organization of the bone mineral. The observable differences for the various bones in the elephant species studied directly depend on the location and type of bone selected. The information gathered in the present study may help to better understand the mineral properties of large vertebrate bones under diagenetic conditions and their susceptibility to physical–chemical alteration during burial, as well as the implications for future paleontological studies into the differentiation between fossil and recent bones.

References

1. Ngatia, J.N.; Lan, T.M.; Ma, Y.; Dinh, T.D.; Wang, Z.; Dahmer, T.D.; Xu, Y.C. Distinguishing extant elephants ivory from mammoth ivory using a short sequence of cytochrome b gene. *Sci. Rep.* **2019**, *9*, 18863. [CrossRef] [PubMed]
2. Hauenstein, S.; Kshatriya, M.; Blanc, J.; Dormann, C.F.; Beale, C.M. African elephant poaching rates correlate with local poverty, national corruption and global ivory price. *Nat. Commun.* **2019**, *10*, 2242. [CrossRef] [PubMed]
3. *The IUCN Red List of Threatened Species*; Version 2020; International Union for Conservation of Nature: Gland, Switzerland, 2020.
4. Roca, A.L.; Ishida, Y.; Brandt, A.L.; Benjamin, N.R.; Zhao, K.; Georgiadis, N.J. Elephant natural history: A genomic perspective. *Annu. Rev. Anim. Biosci.* **2015**, *3*, 139–167. [CrossRef] [PubMed]
5. Miller, W.; Drautz, D.I.; Ratan, A.; Pusey, B.; Qi, J.; Lesk, A.M.; Tomsho, L.P.; Packard, M.D.; Zhao, F.; Sher, A. Sequencing the nuclear genome of the extinct woolly mammoth. *Nature* **2008**, *456*, 387–390. [CrossRef] [PubMed]
6. Lima-Ribeiro, M.S.; Nogués-Bravo, D.; Marske, K.A.; Fernandez, F.A.S.; Araujo, B.; Diniz-Filho, J.A.F. Human arrival scenarios have a strong influence on interpretations of the late Quaternary extinctions. *Proc. Natl. Acad. Sci. USA* **2012**, *109*, E2409–E2410. [CrossRef]
7. Fiedel, S. Sudden deaths: The chronology of terminal Pleistocene megafaunal extinction. In *American Megafaunal Extinctions at the End of the Pleistocene*; Springer: Berlin/Heidelberg, Germany, 2009; pp. 21–37.
8. Moss, C.J. The demography of an African elephant (Loxodonta africana) population in Amboseli, Kenya. *J. Zool.* **2001**, *255*, 145–156. [CrossRef]
9. Locke, M. Structure of ivory. *J. Morphol.* **2008**, *269*, 423–450. [CrossRef]
10. Schmidt-Nielsen, K.; Knut, S.-N. *Scaling: Why Is Animal Size So Important?* Cambridge University Press: Singapore, 1984; ISBN 0521319870.
11. Dove, P.M.; De Yoreo, J.J.; Weiner, S. *Biomineralization*; Mineralogical Society of America: Chantilly, VA, USA, 2003; Volume 54, p. 381.
12. Mann, S. *Biomineralization: Principles and Concepts in Bioinorganic Materials Chemistry*; Oxford University Press: Oxford, UK, 2001.
13. Hadjidakis, D.J.; Androulakis, I.I. Bone remodeling. *Ann. N. Y. Acad. Sci.* **2006**, *1092*, 385–396. [CrossRef]
14. Dominguez-Gasca, N.; Benavides-Reyes, C.; Sánchez-Rodríguez, E.; Rodríguez-Navarro, A.B. Changes in avian cortical and medullary bone mineral composition and organization during acid-induced demineralization. *Eur. J. Mineral.* **2019**, *31*, 209–216. [CrossRef]
15. Grunenwald, A.; Keyser, C.; Sautereau, A.-M.; Crubézy, E.; Ludes, B.; Drouet, C. Revisiting carbonate quantification in apatite (bio) minerals: A validated FTIR methodology. *J. Archaeol. Sci.* **2014**, *49*, 134–141. [CrossRef]
16. Hedges, R.E.M. Bone diagenesis: An overview of processes. *Archaeometry* **2002**, *44*, 319–328. [CrossRef]
17. Rodriguez-Navarro, A.B.; McCormack, H.M.; Fleming, R.H.; Alvarez-Lloret, P.; Romero-Pastor, J.; Dominguez-Gasca, N.; Prozorov, T.; Dunn, I.C. Influence of physical activity on tibial bone material properties in laying hens. *J. Struct. Biol.* **2018**, *201*, 36–45. [CrossRef]
18. Álvarez-Lao, D.J.; Kahlke, R.-D.; García, N.; Mol, D. The Padul mammoth finds—On the southernmost record of Mammuthus primigenius in Europe and its southern spread during the Late Pleistocene. *Palaeogeogr. Palaeoclimatol. Palaeoecol.* **2009**, *278*, 57–70. [CrossRef]

19. García-Alix, A.; Huertas, A.D.; Suárez, E.M. Unravelling the Late Pleistocene habitat of the southernmost woolly mammoths in Europe. *Quat. Sci. Rev.* **2012**, *32*, 75–85. [CrossRef]

20. ICDD PDF-2 Database of the International Center for Diffraction Data (Pennsylvania, USA). 1996. Available online: https://www.icdd.com/pdf-2/ (accessed on 18 August 2022).

21. Rietveld, H.M. A profile refinement method for nuclear and magnetic structures. *J. Appl. Crystallogr.* **1969**, *2*, 65–71. [CrossRef]

22. Rodríguez-Carvajal, J. Recent advances in magnetic structure determination by neutron powder diffraction. *Physica B Condens. Matter Physica B* **1993**, *192*, 55–69. [CrossRef]

23. Wojdyr, M. Fityk: A general-purpose peak fitting program. *J. Appl. Crystallogr.* **2010**, *43*, 1126–1128. [CrossRef]

24. Rey, C.; Collins, B.; Goehl, T.; Dickson, I.R.; Glimcher, M.J. The carbonate environment in bone mineral: A resolution-enhanced Fourier transform infrared spectroscopy study. *Calcif. Tissue Int.* **1989**, *45*, 157–164. [CrossRef]

25. Donnelly, E.; Boskey, A.L.; Baker, S.P.; Van Der Meulen, M.C.H. Effects of tissue age on bone tissue material composition and nanomechanical properties in the rat cortex. *J. Biomed. Mater. Res. Part A Off. J. Soc. Biomater. Jpn. Soc. Biomater. Aust. Soc. Biomater. Korean Soc. Biomater.* **2010**, *92*, 1048–1056. [CrossRef]

26. Lafuente, B.; Downs, R.T.; Yang, H.; Stone, N. 1. The power of databases: The RRUFF project. In *Highlights in Mineralogical Crystallography*; De Gruyter (O): Berlin, Germany, 2015; pp. 1–30, ISBN 3110417103.

27. Peters, F.; Schwarz, K.; Epple, M. The structure of bone studied with synchrotron X-ray diffraction, X-ray absorption spectroscopy and thermal analysis. *Thermochim. Acta* **2000**, *361*, 131–138. [CrossRef]

28. Venkateswarlu, K.; Sandhyarani, M.; Nellaippan, T.A.; Rameshbabu, N. Estimation of crystallite size, lattice strain and dislocation density of nanocrystalline carbonate substituted hydroxyapatite by X-ray peak variance analysis. *Procedia Mater. Sci.* **2014**, *5*, 212–221. [CrossRef]

29. Rodriguez-Navarro, C.; Ruiz-Agudo, E.; Luque, A.; Rodriguez-Navarro, A.B.; Ortega-Huertas, M. Thermal decomposition of calcite: Mechanisms of formation and textural evolution of CaO nanocrystals. *Am. Mineral.* **2009**, *94*, 578–593. [CrossRef]

30. Lozano, L.F.; Pena-Rico, M.A.; Heredia, A.; Ocotlan-Flores, J.; Gomez-Cortes, A.; Velazquez, R.; Belio, I.A.; Bucio, L. Thermal analysis study of human bone. *J. Mater. Sci.* **2003**, *38*, 4777–4782. [CrossRef]

31. Mackie, E.J. Osteoblasts: Novel roles in orchestration of skeletal architecture. *Int. J. Biochem. Cell Biol.* **2003**, *35*, 1301–1305. [CrossRef]

32. Burger, E.H.; Klein-Nulend, J. Mechanotransduction in bone—Role of the lacunocanalicular network. *FASEB J.* **1999**, *13*, S101–S112. [CrossRef]

33. Weinbaum, S.; Cowin, S.C.; Zeng, Y. A model for the excitation of osteocytes by mechanical loading-induced bone fluid shear stresses. *J. Biomech.* **1994**, *27*, 339–360. [CrossRef]

34. Klein-Nulend, J.; Bacabac, R.G.; Mullender, M.G. Mechanobiology of bone tissue. *Pathol. Biol.* **2005**, *53*, 576–580. [CrossRef]

35. McNamara, L.M. 2.10 Bone as a Material. *Compr. Biomater.* **2017**, *2*, 202–227.

36. Benavides-Reyes, C.; Rodriguez-Navarro, A.B.; McCormack, H.A.; Eusemann, B.K.; Dominguez-Gasca, N.; Alvarez-Lloret, P.; Fleming, R.H.; Petow, S.; Dunn, I.C. Comparative analysis of the morphology, chemistry and structure of the tibiotarsus, humerus and keel bones in laying hens. *Br. Poult. Sci.* **2021**, *62*, 795–803. [CrossRef]

37. Torres Pérez-Hidalgo, T.J. Un nuevo sondeo de investigación paleoambiental del Pleistoceno y Holoceno en la turbera del Padul (Granada, Andalucía). *Geogaceta* **1998**, *23*, 99–102.

38. Ortiz, J.E.; Torres, T.; Delgado, A.; Julia, R.; Lucini, M.; Llamas, F.J.; Reyes, E.; Soler, V.; Valle, M. The palaeoenvironmental and palaeohydrological evolution of Padul Peat Bog (Granada, Spain) over one million years, from elemental, isotopic and molecular organic geochemical proxies. *Org. Geochem.* **2004**, *35*, 1243–1260. [CrossRef]

39. Ortner, D.J.; Turner-Walker, G. The biology of skeletal tissues. In *Identification of Pathological Conditions in Human Skeletal Remains*; Elsevier: Amsterdam, The Netherlands, 2003; pp. 11–35.

40. Sillen, A.; LeGeros, R. Solubility profiles of synthetic apatites and of modern and fossil bones. *J. Archaeol. Sci.* **1991**, *18*, 385–397. [CrossRef]

41. Von Endt, D.W.; Ortner, D.J. Experimental effects of bone size and temperature on bone diagenesis. *J. Archaeol. Sci.* **1984**, *11*, 247–253. [CrossRef]

42. Lyman, R.L. Bone density and bone attrition. In *Manual of Forensic Taphonomy*; CRC Press: Boca Raton, FL, USA, 2014; pp. 51–72.

43. Trueman, C.N.G.; Behrensmeyer, A.K.; Tuross, N.; Weiner, S. Mineralogical and compositional changes in bones exposed on soil surfaces in Amboseli National Park, Kenya: Diagenetic mechanisms and the role of sediment pore fluids. *J. Archaeol. Sci.* **2004**, *31*, 721–739. [CrossRef]

44. Smith, C.I.; Craig, O.E.; Prigodich, R.V.; Nielsen-Marsh, C.M.; Jans, M.M.E.; Vermeer, C.; Collins, M.J. Diagenesis and survival of osteocalcin in archaeological bone. *J. Archaeol. Sci.* **2005**, *32*, 105–113. [CrossRef]

45. Trueman, C.N. Chemical taphonomy of biomineralized tissues. *Palaeontology* **2013**, *56*, 475–486. [CrossRef]

46. Reiche, I.; Vignaud, C.; Menu, M. The crystallinity of ancient bone and dentine: New insights by transmission electron microscopy. *Archaeometry* **2002**, *44*, 447–459. [CrossRef]

47. Weiner, S.; Bar-Yosef, O. States of preservation of bones from prehistoric sites in the Near East: A survey. *J. Archaeol. Sci.* **1990**, *17*, 187–196. [CrossRef]

48. Qi, L.; Yuan, X.; Cao, S. Representation and Application of Infrared Reflection Spectra of Gems. *J. Gems Gemmol.* **2005**, *7*, 21–25.

49. Yin, Z.; Zhang, P.; Chen, Q.; Luo, Q.; Zheng, C.; Li, Y. A Comparison of Modern and Fossil Ivories Using Multiple Techniques. *Gems Gemol.* **2013**, *49*, 16–27. [CrossRef]

50. Labs-Hochstein, J.; MacFadden, B.J. Quantification of diagenesis in Cenozoic sharks: Elemental and mineralogical changes. *Geochim. Cosmochim. Acta* **2006**, *70*, 4921–4932. [CrossRef]

51. Rey, C.; Marsan, O.; Combes, C.; Drouet, C.; Grossin, D.; Sarda, S. Characterization of calcium phosphates using vibrational spectroscopies. *Adv. Calcium Phosphate Biomater.* **2014**, 229–266. [CrossRef]

52. Madupalli, H.; Pavan, B.; Tecklenburg, M.M.J. Carbonate substitution in the mineral component of bone: Discriminating the structural changes, simultaneously imposed by carbonate in A and B sites of apatite. *J. Solid State Chem.* **2017**, *255*, 27–35. [CrossRef]

53. Roche, D.; Ségalen, L.; Balan, E.; Delattre, S. Preservation assessment of Miocene–Pliocene tooth enamel from Tugen Hills (Kenyan Rift Valley) through FTIR, chemical and stable-isotope analyses. *J. Archaeol. Sci.* **2010**, *37*, 1690–1699. [CrossRef]

54. Pfretzschner, H.-U. Fossilization of Haversian bone in aquatic environments. *Comptes Rendus Palevol* **2004**, *3*, 605–616. [CrossRef]

55. Machel, H.G. Bacterial and thermochemical sulfate reduction in diagenetic settings—Old and new insights. *Sediment. Geol.* **2001**, *140*, 143–175. [CrossRef]

56. Pfretzschner, H.-U. Pyrite formation in Pleistocene bones-a case of very early mineral formation during diagenesis. *Neues Jahrb. Für Geol. Paläontologie-Abhandlungen* **2000**, *217*, 143–160. [CrossRef]

57. Nielsen-Marsh, C.M.; Hedges, R.E.M. Patterns of diagenesis in bone I: The effects of site environments. *J. Archaeol. Sci.* **2000**, *27*, 1139–1150. [CrossRef]

58. Lyman, R.L. Bone density and differential survivorship of fossil classes. *J. Anthropol. Archaeol.* **1984**, *3*, 259–299. [CrossRef]

59. Nicholson, R.A. Bone degradation, burial medium and species representation: Debunking the myths, an experiment-based approach. *J. Archaeol. Sci.* **1996**, *23*, 513–533. [CrossRef]

60. Kendall, C.; Eriksen, A.M.H.; Kontopoulos, I.; Collins, M.J.; Turner-Walker, G. Diagenesis of archaeological bone and tooth. *Palaeogeogr. Palaeoclimatol. Palaeoecol.* **2018**, *491*, 21–37. [CrossRef]